

# Attenuation Correction Synthesis for Hybrid PET-MR Scanners: Application to Brain Studies

Ninon Burgos\*, M. Jorge Cardoso, Kris Thielemans, Marc Modat, Stefano Pedemonte, John Dickson, Anna Barnes, Rebekah Ahmed, Colin J. Mahoney, Jonathan M. Schott, John S. Duncan, David Atkinson, Simon R. Arridge, Brian F. Hutton, and Sébastien Ourselin

**Abstract**—Attenuation correction is an essential requirement for quantification of positron emission tomography (PET) data. In PET/CT acquisition systems, attenuation maps are derived from computed tomography (CT) images. However, in hybrid PET/MR scanners, magnetic resonance imaging (MRI) images do not directly provide a patient-specific attenuation map. The aim of the proposed work is to improve attenuation correction for PET/MR scanners by generating synthetic CTs and attenuation maps. The synthetic images are generated through a multi-atlas information propagation scheme, locally matching the MRI-derived patient's morphology to a database of MRI/CT pairs, using a local image similarity measure. Results show significant improvements in CT synthesis and PET reconstruction accuracy when compared to a segmentation method using an ultrashort-echo-time MRI sequence and to a simplified atlas-based method.

**Index Terms**—Attenuation correction, image synthesis, positron emission tomography/magnetic resonance (PET/MR).

## I. INTRODUCTION

POSITRON emission tomography/magnetic resonance imaging (PET/MR) scanners are expected to offer a new range of applications in neuro-oncology, epilepsy and neurodegenerative diseases such as Alzheimer's disease [1]. To quantify accurately the radionuclide uptake, PET data need to be corrected for photon attenuation. The attenuation information is usually obtained from a transmission scan in standalone PET or derived from a computed tomography (CT) image in combined PET/CT systems. Regarding PET/MR scanners, the strong magnetic field and the limited bore diameter of the MRI prevent the use of a transmission source. As MRI image intensities do not reflect the electron densities, alternative methods must be developed for PET/MR acquisitions. These methods can be classified into three main categories: emission, segmentation, and atlas-based approaches [2].

The first class of methods exploits information in the PET emission data to estimate the attenuation maps. For instance, recent work looked into joint reconstruction of emission and attenuation, potentially regularized using anatomical information from MRI images [3], [4]. It has been suggested that, for certain tracers, inclusion of time-of-flight information improves this type of approach [4], [5].

In segmentation-based methods, uniform linear attenuation coefficients are assigned to tissue classes obtained by segmenting an MRI image. In the method from Martinez-Möller *et al.* [6], the body is segmented into four classes: background, lungs, fat, and soft-tissues. While the results obtained in whole-body studies are satisfactory, the lack of bone information has a significant impact on the quantification of the radionuclide uptake in brain studies [7]. Catana *et al.* [8], Keereman *et al.* [9], and more recently Aitken *et al.* [10], used ultrashort-echo-time (UTE) MRI sequences to distinguish cortical bone, air, and soft tissue, which improves the accuracy of the results. Berker *et al.* [11] developed a four-class tissue segmentation technique applied to brain studies. Cortical bone, air, fat, and soft-tissues are segmented using a combined UTE/Dixon MRI sequence. Although the achieved overall voxel classification accuracy is superior to the accuracy obtained without Dixon or UTE components, the bone segmentation is still inaccurate in complex regions such as nasal sinuses [11]. Recently, Yang *et al.* [12] proposed a skull

Manuscript received May 15, 2014; revised June 27, 2014; accepted July 10, 2014. Date of publication July 17, 2014; date of current version November 25, 2014. This work was supported by an IMPACT studentship funded jointly by Siemens and the UCL Faculty of Engineering Sciences. The Dementia Research Centre is an Alzheimer's Research UK Co-ordinating Centre and has also received equipment funded by Alzheimer's Research UK and Brain Research Trust. S. Ourselin receives funding from the EPSRC (EP/H046410/1, EP/J020990/1, EP/K005278), the MRC (MR/J01107X/1), the EU-FP7 project VPH-DARE@IT (FP7-ICT-2011-9-601055), and the NIHR Biomedical Research Unit (Dementia) at UCL. This work was also supported by AVID Radiopharmaceuticals (a wholly owned subsidiary of Eli Lilly) and by researchers at the National Institute for Health Research University College London Hospitals Biomedical Research Centre (NIHR BRC UCLH/UCL High Impact Initiative). *Asterisk indicates corresponding author.*

\*N. Burgos is with the Centre for Medical Image Computing and the Institute of Nuclear Medicine, University College London, WC1E 6BT London, U.K. (e-mail: n.burgos.12@ucl.ac.uk).

M. J. Cardoso, M. Modat, and S. Ourselin are with Centre for Medical Image Computing and the Dementia Research Centre, University College London, WC1E 6BT London, U.K.

K. Thielemans, J. Dickson, and A. Barnes are with the Institute of Nuclear Medicine, University College London, NW1 2BU London, U.K.

S. Pedemonte was with the Centre for Medical Image Computing, University College London, WC1E 6BT London, U.K.. He is now with the Martinos Center for Biomedical Imaging, Massachusetts General Hospital, Harvard Medical School, Charlestown, MA 02129 USA, and also with the Departments of Information and Computer Science and of Biomedical Engineering and Computational Science, Aalto University, FI-00076 Aalto, Finland.

R. Ahmed, C. Mahoney, and J. M. Schott are with the Dementia Research Centre, University College London, WC1N 3AR London, U.K.

J. S. Duncan is with Department of Clinical and Experimental Epilepsy, University College London, WC1N 3BG London, U.K.

D. Atkinson is with the Centre for Medical Imaging, University College London, WC1E 6JF London, U.K.

S. R. Arridge is with the Centre for Medical Image Computing, University College London, WC1E 6BT London, U.K.

B. F. Hutton is with Institute of Nuclear Medicine, University College London, NW1 2BU London, U.K., and also the Centre for Medical Radiation Physics, University of Wollongong, Wollongong NSW 2522, Australia.

Color versions of one or more of the figures in this paper are available online at <http://ieeexplore.ieee.org>.

Digital Object Identifier 10.1109/TMI.2014.2340135

segmentation method for T1-weighted MRI images via a multiscale bilateral filtering processing of MRI sinogram data in the Radon domain. Even though generally robust and accurate, this method encounters difficulties differentiating bone and air in the sinuses.

In atlas-based methods, an anatomical model or dataset is deformed to match the patient's anatomy in order to apply the attenuation map from the model to the patient data. Schreibmann *et al.* [13] developed a multimodality optical flow deformable model that maps patient MRI images to a CT atlas. The CT atlas is then warped with the deformation field obtained by the registration to generate a simulated CT image that matches the patient anatomy. Johansson *et al.* [14] described a Gaussian mixture regression model that links the MRI intensity values to the CT Hounsfield units (HU). Assuming a correspondence between MRI and CT intensities can lead to estimation errors as several materials such as cerebrospinal fluid, air, and bone have similar low intensities in a T1-weighted MRI image but distinct values in a CT image. Considering spatial information may enhance the results of such techniques, but inaccuracies still remain at boundaries such as air and bone in the nasal sinuses [15]. In the Hofmann *et al.* method [16], local information derived from a pattern recognition technique and global information obtained by an atlas registration are combined to predict a pseudo-CT image from a given MRI image. Navalpakkam *et al.* [17] used a CT image acquired with a PET/CT scanner and images of the same patient derived from 3-D Dixon-volume interpolated breath-hold examination and UTE MRI sequences acquired with a PET/MR scanner to derive a pseudo CT using an epsilon-insensitive support vector regression. These techniques enable the synthesis of continuous valued attenuation maps.

Combining the segmentation of an MRI image and the use of a CT image database, Marshall *et al.* [18] proposed a method to correct for attenuation whole-body PET/MR scans. The subject's MRI is compared to a database of CT images using a set of 19 similarity metrics such as gender, age, and body, lung, and bone geometries. The most similar CT image is nonrigidly aligned to the subject's MRI. Bones from the registered CT image are then added to the MRI image previously segmented into four tissue classes (air, lung, fat, and lean tissue).

The main weakness of the MRI-based attenuation correction methods is the lack of accuracy of the bone delineation as both bone and air have similar low intensities in MRI images. However, these inaccuracies lead to a strong spatial bias of the PET activity as shown in [19] and [20]. The proposed method follows the principle of multi-atlas propagation to synthesize an attenuation correction map from an MRI image. As an alternative to a one-to-one mapping from the observed MRI intensities to CT-like intensities, one can exploit the concept of morphological similarity between subjects. When used in the context of segmentation propagation [21], a set of segmented anatomical atlases from several subjects are mapped to a target subject and subsequently fused according to the morphological similarity between the mapped and the target anatomical images. This morphological similarity, normally interpreted as an image similarity measure, is used to enforce the fact that the most morphologically similar atlases should carry more weight during the fusion process [22]. This work will exploit the same idea, but for the propagation and fusion of continuous image intensities. The

developed algorithm makes use of a pre-acquired set of aligned MRI/CT image pairs from multiple subjects to propagate, in a voxel wise fashion, the CT intensities corresponding to similar MRIs. The proposed approach relies on the concept of morphological similarity rather than the assumption of one-to-one intensity mapping between the MRI and the CT. This enables the synthesis of a patient-specific pseudo CT image, from which the attenuation map is then generated. This paper is an extension of preliminary work [23].

## II. METHOD

In PET/CT imaging, the main technique to correct for attenuation is to derive the attenuation coefficients from a CT image. In the case of a hybrid PET/MR scanner, the only anatomical and structural information available are MRI images. A diagram illustrating the proposed method in which a synthetic CT is obtained from a given MRI is shown in Fig. 1.

### A. MRI-CT Database Preprocessing and Inter-Subject Mapping

The atlas database consisted of pairs of T1-weighted MRI and CT brain images. T1 images were corrected for intensity nonuniformity following a nonparametric nonuniform intensity normalization method [24]. CT images were segmented to separate the head from the bed using thresholding and morphological operators.

For each subject, the MRI was affinely aligned to the CT using a symmetric approach [25] based on Ourselin *et al.* [26]. Even though this is an intra-subject alignment, a full affine registration was used to compensate for possible gradient drift and calibration in the MRI scans.

In order to synthesize the CT from a given MRI, one first needs to register all the MRIs from the atlas database to the target MRI. This inter-subject coordinate mapping was obtained using a symmetric global registration followed by a cubic B-spline parametrized nonrigid registration, using normalized mutual information as a measure of similarity [27]. All the CTs in the atlas database were then mapped to the target subject using the transformation that maps the subject's corresponding MRI in the atlas database to the target MRI. Through this registration and resampling procedure, one obtains a series of MRI/CT pairs aligned to the MRI of the target subject.

### B. CT Synthesis

The proposed framework uses a local image similarity measure between the target MRI and the set of registered MRIs as a metric of the underlying morphological similarity. Provided the local image intensity is a good approximation of the local morphological similarity between subjects, we assume that if two MRIs are similar at a certain spatial location, the two CTs will also be similar at this location.

1) *Image/Morphological Similarity*: The similarity measure monitors the local quality of match between the MRI of the target subject and each of the warped MRIs from the atlas database. In this work, two similarity measures were tested: the convolution-based fast local normalized correlation coefficient (LNCC) proposed by Cachier *et al.* [28] and the local normalized sum of square differences (NSSD). The LNCC evaluates

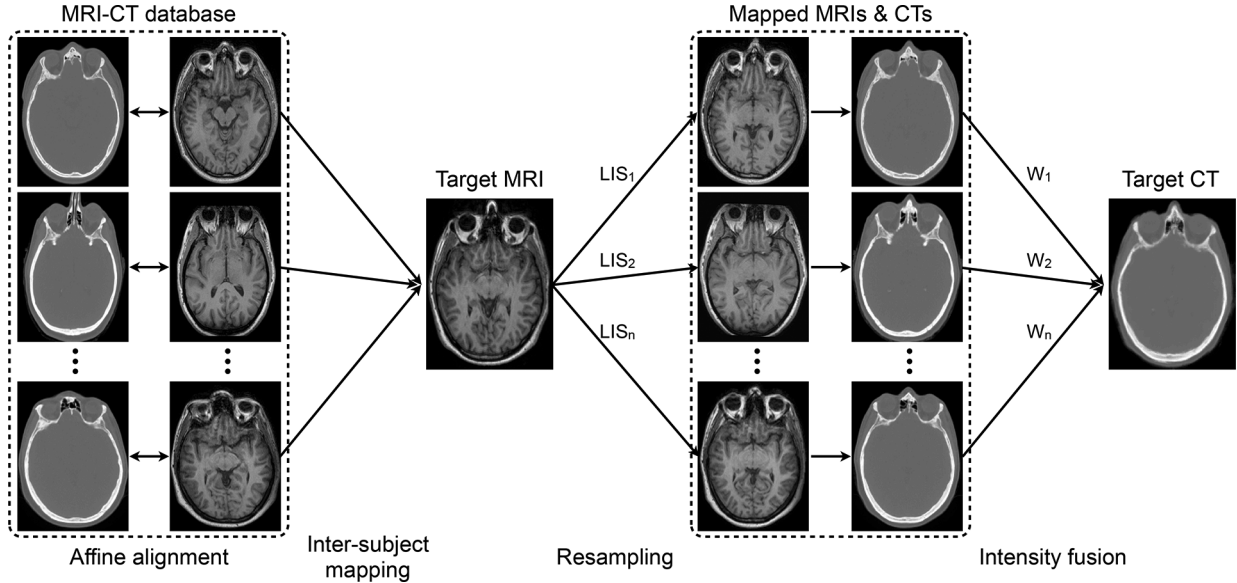


Fig. 1. CT synthesis diagram for a given MRI image. All the MRIs in the atlas database are registered to the target MRI. The CTs in the atlas database are then mapped using the same transformation to the target MRI. A local image similarity measure (LIS) between the mapped and target MRIs is converted to weights ( $W$ ) to reconstruct the target CT.

the quality of alignment between two images by calculating the correlation between the signals, with a larger focus on high contrast regions, while the NSSD characterises the differences in intensity between the two images, making it more susceptible to contrast problems.

Let the target subject's MRI be denoted by  $I^{\text{MRI}}$  and its corresponding unknown CT be denoted by  $I^{\text{CT}}$ . For each of the  $N$  atlases in the database, let the mapped MRI and CT images of atlas  $n$  be denoted by  $J_n^{\text{MRI}}$  and  $J_n^{\text{CT}}$ , respectively. The LNCC between  $I^{\text{MRI}}$  and  $J_n^{\text{MRI}}$  at voxel  $\vec{v}$  is then given by

$$\text{LNCC}_{n,\vec{v}} = \frac{\langle I^{\text{MRI}}, J_n^{\text{MRI}} \rangle_{\vec{v}}}{\sigma(I^{\text{MRI}})_{\vec{v}} \sigma(J_n^{\text{MRI}})_{\vec{v}}}. \quad (1)$$

As in [28], the means and standard deviations at voxel  $\vec{v}$  were calculated using a Gaussian kernel  $G_{\sigma_G}$  with standard deviation  $\sigma_G$  through convolution

$$\begin{aligned} \bar{I}_{\vec{v}} &= [G_{\sigma_G} * I]_{\vec{v}} & \sigma(I)_{\vec{v}} &= \sqrt{\bar{I}^2_{\vec{v}} - \bar{I}^2_{\vec{v}}} \\ \langle I, J \rangle_{\vec{v}} &= \bar{I} \cdot \bar{J}_{\vec{v}} - \bar{I}_{\vec{v}} \cdot \bar{J}_{\vec{v}} \end{aligned}$$

where  $*$  denotes the convolution operator. High LNCC values indicate a better local match between the two MRI images. The NSSD is given by

$$\text{NSSD}_{n,\vec{v}} = \left[ G_{\sigma_G} * \left( \frac{I^{\text{MRI}} - \bar{I}^{\text{MRI}}}{\sigma(I^{\text{MRI}})} - \frac{J_n^{\text{MRI}} - \bar{J}_n^{\text{MRI}}}{\sigma(J_n^{\text{MRI}})} \right) \right]_{\vec{v}}^2 \quad (2)$$

where  $G_{\sigma_G}$  is a Gaussian kernel with standard deviation  $\sigma_G$ . Low NSSD values indicate a better local match between the two MRI images.

A ranking scheme similar to the one proposed by Yushkevich *et al.* [29] was used to compensate for registration inaccuracies, giving a larger weight to the images better registered to the target image. The LNCC and NSSD at each voxel were ranked across

all atlas images, with the rank being denoted by  $R_{n\vec{v}}$ . The ranks  $R_{n\vec{v}}$  were then converted to weights by applying an exponential decay function

$$W_{n,\vec{v}} = e^{-\beta R_{n\vec{v}}} \quad (3)$$

with  $W_{n\vec{v}}$  being the weight associated with the  $n$ th subject image at voxel  $\vec{v}$ . With the ranking strategy, the sum and separation of the weights for different voxels are the same at every voxel location, which increases the algorithm's ability to discriminate between atlases in regions with low contrast and leads to better results.

2) *Intensity Fusion*: Similarly to the label fusion framework suggested by Cardoso *et al.* [30], an estimate of the target subject's CT can be obtained by a spatially varying weighted averaging. The weights  $W_{n\vec{v}}$  were used to reconstruct the target CT image  $I^{\text{CT}}$  at voxel  $\vec{v}$  as follows:

$$I_{\vec{v}}^{\text{CT}} = \frac{\sum_{n=1}^N W_{n\vec{v}} \cdot J_n^{\text{CT}}}{\sum_{n=1}^N W_{n\vec{v}}}. \quad (4)$$

### C. Attenuation Map

To obtain the attenuation map ( $\mu$ -map), the CT values expressed in HU were converted to linear attenuation coefficients in  $\text{cm}^{-1}$  by a piecewise linear transformation [31]

$$\mu = \begin{cases} \mu_{\text{water}} \left( 1 + \frac{I^{\text{CT}}}{1000} \right) & I^{\text{CT}} \leq 0 \text{ HU} \\ \mu_{\text{water}} \left( 1 + \frac{I^{\text{CT}}}{1000} \frac{\rho_{\text{bone}}(\mu_{\text{bone}} - \mu_{\text{water}})}{\mu_{\text{water}}(\rho_{\text{bone}} - \rho_{\text{water}})} \right) & I^{\text{CT}} > 0 \text{ HU} \end{cases} \quad (5)$$

where  $\mu_{\text{water}}$  and  $\mu_{\text{bone}}$  represent the attenuation coefficients at the PET 511 keV energy for water and bone respectively and  $\rho_{\text{water}}$  and  $\rho_{\text{bone}}$  represent the attenuation coefficients at the CT energy (120 keV), respectively. These values were set to  $\mu_{\text{water}} = 0.096 \cdot \text{cm}^{-1}$ ,  $\mu_{\text{bone}} = 0.172 \cdot \text{cm}^{-1}$ ,  $\rho_{\text{water}} = 0.158 \cdot$

$\text{cm}^{-1}$  and  $\rho_{\text{bone}} = 0.326 \cdot \text{cm}^{-1}$ . The synthetic CT image was then smoothed using a Gaussian filter with a kernel standard deviation of 2 voxels ( $1.172 \times 1.172 \times 2.5 \text{ mm}^3$ ) to approximate the PET's point spread function (PSF), and resampled to the PET's discretization grid. This method is widely accepted to generate attenuation maps from CT images, as an alternative to methods exploiting transmission scans, when the subject does not present metal implants. The transformation accuracy can be improved by adjusting the attenuation coefficient of water to the scanner used [31], [32].

### III. VALIDATION AND RESULTS

#### A. Data

Two distinct datasets were used in this work. The first dataset is used for the optimization of the parameters and the second dataset for the validation. Subjects from the first and second datasets were part of an Alzheimer's disease study and an epilepsy study, respectively, and do not present unusual anatomy.

1) *Parameter Optimization*: The dataset dedicated to the parameter optimization was composed of 18 brain T1-weighted MRIs and CTs. The T1-weighted MRIs (3.0 T; TE/TR/TI, 2.9 ms/2200 ms/900 ms; flip angle  $10^\circ$ ; voxel size  $1.1 \times 1.1 \times 1.1 \text{ mm}^3$ ) were acquired on a Siemens Magnetom Trio scanner; the CTs (voxel size  $0.586 \times 0.586 \times 2.5 \text{ mm}^3$ , 120 kVp, 300 mA) on a GE Discovery ST PET/CT scanner.

2) *Validation*: The dataset used for the validation was composed of 41 brain T1-weighted MRIs, CTs, UTE-based  $\mu$ -maps and reconstructed PETs, and one PET sinogram. The T1-weighted MRIs (3.0 T; TE/TR/TI, 2.63 ms/1700 ms/900 ms; flip angle  $9^\circ$ ; voxel size  $0.53 \times 0.53 \times 1.1 \text{ mm}^3$ ), UTE-based  $\mu$ -maps (voxel size  $1.562 \times 1.562 \times 1.562 \text{ mm}^3$ ) and PET sinogram (radiopharmaceutical: FDG) were acquired on a Siemens Biograph mMR hybrid PET/MR scanner; the CTs (voxel size  $0.586 \times 0.586 \times 1.25 \text{ mm}^3$ , 120 kVp, 300 mA) and reconstructed PETs (radiopharmaceutical: FDG; voxel size  $1.953 \times 1.953 \times 3.27 \text{ mm}^3$ ) on a GE Discovery ST PET/CT scanner. 250 MBq of FDG were administered half an hour before the 15-min PET/CT examination. The patients were then transferred to the PET/MR scanner for a 15-min PET acquisition.

#### B. Parameter Optimization

The morphological similarity between the target MRI and each of the registered MRIs from the atlas database was assessed using a local image similarity measure. For both the LNCC and NSSD metrics, two parameters were optimized using a leave-one-out cross validation on the 18 subjects from the first dataset: the standard deviation of the Gaussian kernels used in (1) and (2) ( $\sigma_G$ , expressed in voxels)

$$\sigma_G = [1 \quad 3 \quad 5 \quad 7 \quad 9]$$

and  $\beta$  from (3) whose value influences the repartition of the weights

$$\beta = [1 \quad 0.5 \quad 0.25 \quad 0.1 \quad 0.01].$$

The weighted sum tends to the mean when  $\beta$  is small.

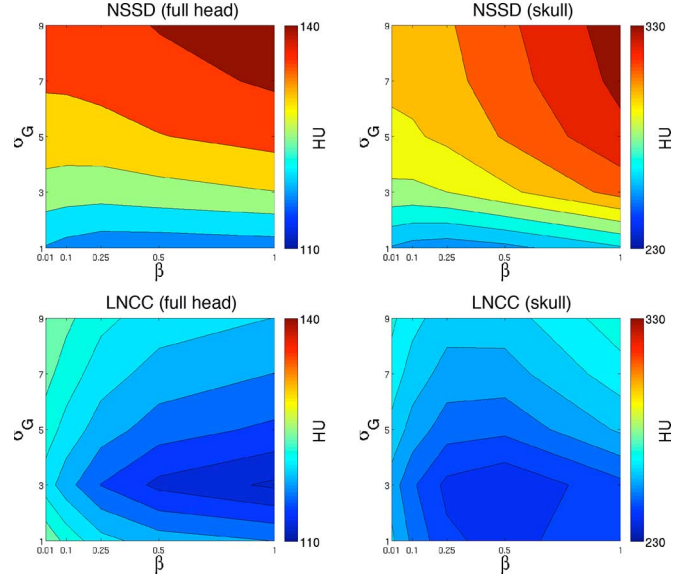


Fig. 2. Average MAE between the ground truth CT and the pseudo CT generated using the LNCC and NSSD as similarity metrics for varying values of  $\sigma_G$  and  $\beta$ . Best parameters are obtained for the LNCC, with  $\sigma_G = 3$  and  $\beta = 0.5$ , giving an average MAE of 113 HU for the full head and 240 HU for the skull region of interest.

Using only the MRI image of the subject, a pseudo CT image ( $I = I^{\text{CT}}$ ) was generated using the proposed method. This synthetic CT was then compared to the ground truth CT ( $GT = GT^{\text{CT}}$ ). The metric employed to measure the synthesis error was the mean absolute error, defined as

$$\text{MAE} = \frac{\sum_{\vec{v}} |I_{\vec{v}} - GT_{\vec{v}}|}{V} \quad (6)$$

where  $V$  is the number of voxels in the region of interest. This cost function was estimated between the ground truth CT and the pseudo CT for every subject in the optimization dataset. The average values of MAE over all subjects are shown in Fig. 2. The optimization focused on two regions: the full head and the skull region, obtained setting a threshold at 100 HU. The skull region is important as bones have the highest attenuation coefficients and can induce large errors.

*Results*: For both the full head and the skull region, the LNCC with  $\sigma_G = 3$  voxels gives the smallest error.  $\beta = 0.5$  is the skull optimum and guarantees smoother images. With these parameters, the average MAE is 113 HU for the full head and 240 HU for the skull region. A large range of parameters was tested in the optimization, all showing small differences in the results. The existence of a plateau in terms of accuracy in the parameter space means that small changes in parameters result in a very similar pseudo CT and indicates that the method is robust to the choice of parameters. For this reason, and to avoid being influenced by other factors, we chose to optimize the parameters using the CT synthesis accuracy rather than the PET reconstruction accuracy.

#### C. Validation Scheme

In order to validate the algorithm with the previously optimized parameters, but on a completely independent dataset, the performance of the proposed synthesis algorithm was ran

against ground truth data for 41 subjects. We also compared it to two other methods: a UTE-based method obtained through MRI segmentation and a simplified atlas-based method.

The UTE-based method uses the segmentation of a UTE MRI sequence which enables the differentiation of three tissue classes (bone, air, and soft tissue). A prototype version of this method, only made available to early users of the Siemens Biograph mMR hybrid PET/MR scanners, was used in this work. In the following, when the values assigned to the classes are expressed in HU, the image is referred to as UTE CT, and when the values correspond to linear attenuation coefficients in  $\text{cm}^{-1}$ , the image is called UTE  $\mu$ -map and matches the PET's PSF and voxel size.

The second method is based on atlases. As in the proposed method, the database of MRI and CT pairs is nonrigidly registered to the target MRI. A global similarity measure, the normalized cross-correlation (NCC), is computed over the full image field of view between each warped MRI and the target MRI to select the most similar atlas to the target. The NCC is defined as

$$\text{NCC}_n = \frac{1}{V} \left\langle \frac{I^{\text{MRI}} - \overline{I^{\text{MRI}}}, J_n^{\text{MRI}} - \overline{J_n^{\text{MRI}}}}{\sigma(I^{\text{MRI}})\sigma(J_n^{\text{MRI}})} \right\rangle \quad (7)$$

where  $\overline{I}$  is the mean and  $\sigma(I)$  the standard deviation of image  $I$ . The CT corresponding to the selected MRI, called best-atlas CT (baCT), is then converted into attenuation map (baCT  $\mu$ -map), as in the proposed method.

The quantitative validation consisted of three steps.

- 1) A pseudo CT was synthesised from each subject's MRI following the proposed method. The pseudo CT (pCT), baCT, and UTE CT were compared to the subject's ground truth CT image at the original resolution, validating the accuracy of the CT synthesis.
- 2) The pCT, baCT, and UTE CT were converted to attenuation maps using (5), smoothed to approximate the PET's PSF and resampled to the PET's discretization grid, to validate how accurate the synthetic CT was at the resolution relevant for PET reconstruction.
- 3) The PET image was reconstructed from a simulated sinogram using the pCT  $\mu$ -map generated using the proposed method, the baCT  $\mu$ -map and the UTE  $\mu$ -map, and compared with the gold standard PET reconstructed using the CT-based  $\mu$ -map, validating the accuracy of the PET attenuation correction.

The field of view of the MRI images contained the head and neck of the subject while in the CT field of view, only the head was visible. After alignment of the two modalities, the analysis was limited to a mask defined where both image modalities provide information. All quantitative assessments were performed using a leave-one-out cross-validation scheme.

#### D. Results

1) *Pseudo CT Accuracy*: Following the proposed method, a pseudo CT was generated using only the MRI image of the subject, and then compared to the ground truth CT. The MAE, as defined in (6), and the mean error (ME) defined as

$$\text{ME} = \frac{\sum_{\vec{v}} (I_{\vec{v}} - GT_{\vec{v}})}{V} \quad (8)$$

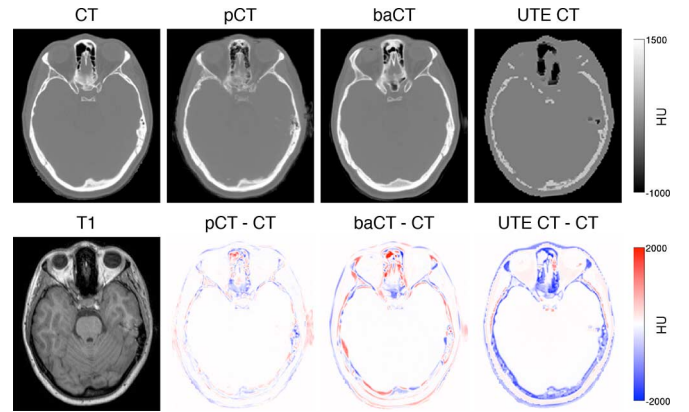


Fig. 3. For subject 1, from left to right: the acquired CT, the pCT generated by the proposed method, the baCT, and the UTE CT (top); the acquired T1, the difference between the pCT and the CT, the difference between the baCT and the CT, and the difference between the UTE CT and the CT (bottom).

were calculated between the ground truth CT and the pseudo CT for every subject in the validation dataset. Contrary to the MAE, which provides information about reconstruction error and deviations from the expected values, the ME provides information about an inherent bias in the methodology. The MAE and ME were also computed between the best-atlas CT and the ground truth CT, and between the UTE CT and the ground truth CT. The average  $\pm$  standard deviation (SD) MAEs and MEs, measured in Hounsfield units, across all the subjects in the database are presented in Table I. The average  $\pm$ SD absolute error obtained with the pseudo CT method ( $121 \pm 17$  HU) is 1.4 times smaller than the error obtained with the best-atlas method ( $172 \pm 23$  HU) and 1.7 times smaller than the error obtained with the UTE method ( $203 \pm 24$  HU). A paired t-test was used to confirm that the improvement is statistically significant ( $p < 10^{-6}$ ) when the proposed method was employed instead of the best-atlas and UTE-based methods. Examples of ground truth CT, pseudo CT, best-atlas CT, UTE CT and difference images are presented in Fig. 3 for a representative subject (subject 1) whose results were close to the average results.

2) *Attenuation Map Accuracy*: The relative mean absolute error between the ground truth  $\mu$ -map ( $GT = GT^{\mu\text{-map}}$ ) and the pseudo CT  $\mu$ -map ( $I = I^{\mu\text{-map}}$ ), defined as

$$\text{rMAE} = 100 * \frac{\sum_{\vec{v}} |I_{\vec{v}} - GT_{\vec{v}}|}{\sum_{\vec{v}} GT_{\vec{v}}} \quad (9)$$

and the relative mean error, defined as

$$\text{rME} = 100 * \frac{\sum_{\vec{v}} (I_{\vec{v}} - GT_{\vec{v}})}{\sum_{\vec{v}} GT_{\vec{v}}} \quad (10)$$

were used to assess the attenuation map synthesis accuracy. The rMAE and rME were also computed between the best-atlas CT  $\mu$ -map and the ground truth CT  $\mu$ -map, and between the UTE  $\mu$ -map and the ground truth CT  $\mu$ -map. The average  $\pm$ SD rMAEs and rMEs, measured in percentages, across all the subjects in the database are presented in Table I. The average  $\pm$ SD absolute error obtained with the pseudo CT method ( $6.6 \pm 1.3\%$ ) is 1.4 times smaller than the error obtained with the best-atlas method ( $9.3 \pm 1.5\%$ ) and half of the error obtained with the UTE

TABLE I

FOR 41 SUBJECTS: AVERAGE AND SD OF THE MAE AND ME BETWEEN THE GROUND TRUTH CT AND BOTH THE PSEUDO CT, BEST-ATLAS CT, AND UTE CT; AVERAGE AND SD OF THE rMAE AND rME BETWEEN THE GROUND TRUTH CT  $\mu$ -MAP AND BOTH THE PSEUDO CT, BEST-ATLAS CT, AND UTE  $\mu$ -MAPS; AVERAGE AND SD OF THE rMAE AND rME BETWEEN THE GOLD STANDARD CT PET AND BOTH THE PSEUDO CT, BEST-ATLAS CT, AND UTE PETS, BEFORE AND AFTER NORMALIZATION, FOR THE BRAIN AND GREY MATTER (GM) REGIONS

		CT (HU) - Head			$\mu$ -map (%) - Head			PET (%) - Brain			Normalised PET (%) - Brain			Normalised PET (%) - GM		
		pCT	baCT	UTE	pCT	baCT	UTE	pCT	baCT	UTE	pCT	baCT	UTE	pCT	baCT	UTE
MAE	Average	121	172	203	6.6	9.3	13.2	2.87	4.30	11.86	2.99	4.76	7.70	2.98	4.80	7.27
	SD	17	23	24	1.3	1.5	1.4	0.90	1.16	2.09	0.98	1.79	1.98	0.97	1.80	1.90
ME	Average	-7.3	5.1	-132	-1.2	-0.1	-10.3	0.17	0.78	-11.78	0.98	1.08	-0.50	0.99	1.17	-0.81
	SD	23	30	34	1.7	2.1	2.1	2.11	2.88	2.13	1.69	3.44	4.91	1.71	3.48	4.80

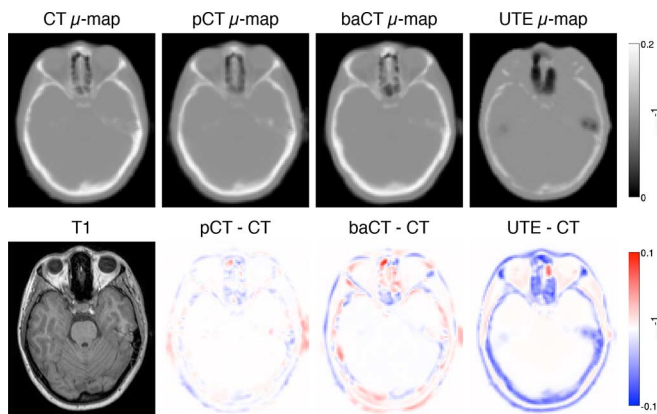


Fig. 4. For subject 1, from left to right: CT  $\mu$ -map, pCT  $\mu$ -map generated by the proposed method, baCT  $\mu$ -map and UTE  $\mu$ -map (top); T1, difference between the pCT and CT  $\mu$ -maps, difference between the baCT and CT  $\mu$ -maps, and difference between the UTE and CT  $\mu$ -maps (bottom).

method ( $13.2 \pm 1.4\%$ ). The paired t-test shows a statistically significant improvement ( $p < 10^{-6}$ ) with the proposed method. Examples of ground truth CT  $\mu$ -map, pseudo CT  $\mu$ -map, best-atlas CT  $\mu$ -map, UTE  $\mu$ -map, and difference images are presented in Fig. 4.

3) *PET Accuracy*: A hardware  $\mu$ -map containing the bed visible in the PET/CT scans, previously extracted from the original CT  $\mu$ -map, was added to the human  $\mu$ -maps (CT, pCT, baCT, and UTE  $\mu$ -maps). Due to the unavailability of the raw PET data, we made use of the PET reconstruction provided by the PET/CT scanner. To reconstruct the PET image with the different  $\mu$ -maps, we followed a projection/reconstruction technique similar to Hofmann *et al.* [16]. The original PET image and the CT  $\mu$ -map were projected to obtain simulated sinograms. The scatter sinogram was estimated using a Single Scatter Simulation algorithm [33]. The attenuation and scatter corrections were subsequently removed from the original simulated PET sinogram producing a noncorrected PET sinogram. The noncorrected PET sinogram was then reconstructed using the CT, pCT, baCT, or UTE  $\mu$ -map to correct for attenuation and scatter. The PET image reconstructed using the CT  $\mu$ -map was considered as the gold standard PET. The iterative reconstruction and scatter estimation were performed using STIR [34]. An ordered subsets expectation maximization (OSEM) algorithm with three iterations of 21 subsets was used. Effects of PSF and randoms were not included and post-reconstruction smoothing was not applied.

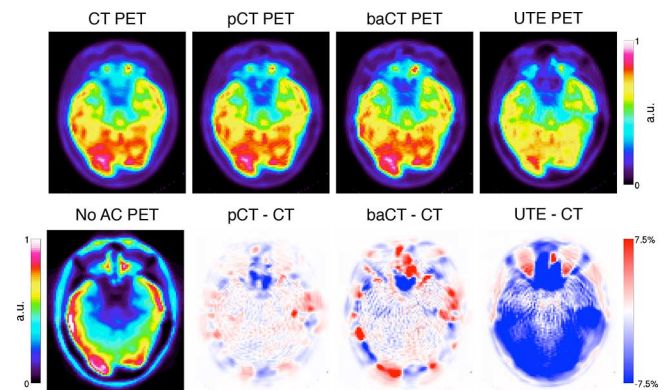


Fig. 5. For subject 1, from left to right: the gold standard FDG PET, the pCT PET, the baCT PET, and the UTE PET (top); the noncorrected PET, the difference between the pCT and CT PETs, the difference between the baCT and CT PETs, and the difference between the UTE and CT PETs (bottom).

Results of PET reconstructions using different attenuation maps and difference images are displayed in Fig. 5. The rMAE was computed between the gold standard PET and the pCT, baCT, and UTE PETs for the brain region. Results are shown in Table I. The average  $\pm$ SD rMAE obtained using the pCT  $\mu$ -map ( $2.87 \pm 0.90\%$ ) is 1.5 times smaller than the error obtained using the baCT  $\mu$ -map ( $4.30 \pm 1.16\%$ ) and 4 times smaller than the error obtained using the UTE  $\mu$ -map ( $11.86 \pm 2.09\%$ ), which represents a statically significant improvement ( $p < 10^{-6}$ ) in reconstruction error.

A common practice in the neuro-imaging community is to normalize PET images using a reference region [35], [36]. For our application, we used the mean PET value in the pons, manually segmented from the T1 image, to normalize the PET images of each subject, allowing for a comparable range of values. The average  $\pm$ SD rMAE obtained for the brain region using the pCT  $\mu$ -map ( $2.99 \pm 0.98\%$ ) is 1.6 times smaller than the error obtained using the baCT  $\mu$ -map ( $4.76 \pm 1.79\%$ ) and 2.6 times smaller than the error obtained using the UTE  $\mu$ -map ( $7.70 \pm 1.98\%$ ), which represents a statically significant improvement ( $p < 10^{-6}$ ). The boxplots in Fig. 7 show that the proposed method is less prone to produce outlier results compared to the best-atlas and UTE methods. We note that while the results obtained for the proposed and best-atlas methods do not vary significantly depending on the normalization of the PET images, the mean absolute error obtained with the UTE method decreases when the PET images are normalized.

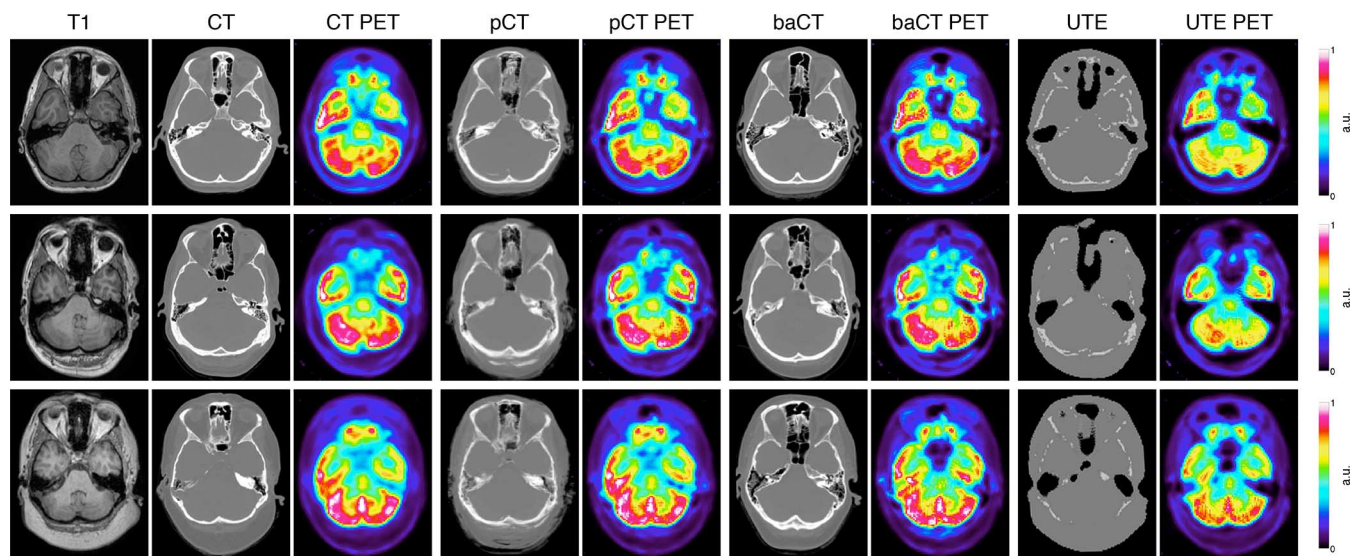


Fig. 6. From left to right: the acquired T1-weighted MRI, CT, and gold standard FDG PET, the pCT, and PET generated by the proposed method, the baCT and PET, and the UTE CT and PET, for the subjects whose pCT PET obtained the lowest (top row), average (middle row), and highest (bottom row) rMAE.

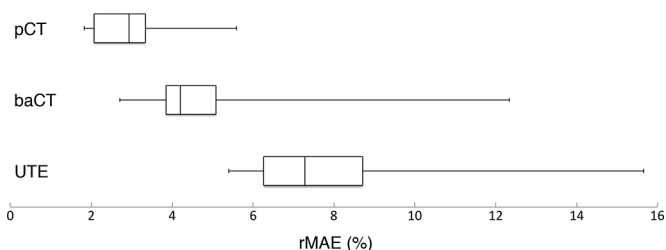


Fig. 7. For 41 subjects: boxplots displaying the median, the lower and upper quartiles and the minimum and maximum of the rMAE calculated between the gold standard CT PET and both the pseudo CT, best-atlas CT, and UTE PETs in the brain after normalization. Similar results were obtained in the grey matter region.

In order to assess the performance of the proposed method in areas close to the skull, we also analyzed results in the grey matter region, which was segmented from the T1 image and propagated to the PET images [37]. The average  $\pm$ SD rMAE obtained using the pCT  $\mu$ -map ( $2.98 \pm 0.97\%$ ) is significantly smaller ( $p < 10^{-6}$ ) than the error obtained using the baCT  $\mu$ -map ( $4.80 \pm 1.80\%$ ) and the UTE  $\mu$ -map ( $7.27 \pm 1.90\%$ ). These results are similar to the ones obtained in the brain region.

Examples of T1, CT, pseudo CT, best-atlas CT, UTE CT, and reconstructed PET images are displayed in Fig. 6 for subjects whose pCT PET obtained the lowest, the average and the highest rMAE.

4) *PET Bias Analysis*: The main goal when correcting for attenuation is to be able to perform an accurate quantitative analysis of PET data. In order to analyze the bias introduced by the different attenuation correction methods in the PET images, the rME was computed between the gold standard PET and the pCT, baCT, and UTE PETs for the brain region. The rME results indicate a reduced bias when the proposed method is used ( $0.17 \pm 2.11\%$ ) compared to the best-atlas ( $0.78 \pm 2.88\%$ ) and UTE-based ( $-11.78 \pm 2.13\%$ ) methods. The Kolmogorov–Smirnov test was used to determine if the bias introduced by the different attenuation correction methods came

from a normal distribution with 0 mean, thus assessing if the mean error was significantly different from 0. Furthermore, as the relative mean errors were Gaussian distributed (according to the Kolmogorov–Smirnov test), the F test was used to determine if the variance of the bias differs between methods. All tests were performed at 0.1% significance level.

In contrast with the baCT and UTE  $\mu$ -maps, where the rME was found to differ significantly from zero, the rME is not significantly different from zero when the pCT  $\mu$ -map is used to correct for attenuation. The variances of the three methods are not significantly different.

When normalized, regardless of the  $\mu$ -map used to correct for attenuation, the bias ( $<1.2\%$ ) is significantly different from zero. However, the variance of the rME is significantly lower when the proposed method is employed instead of the best-atlas or UTE method.

We also performed a linear regression with the expression  $y = \alpha x + \beta$  where  $x$  corresponds to the gold standard, nonnormalized, PET and  $y$  to either the noncorrected, pCT, baCT, or UTE PET. The averages and SDs of the regression coefficients  $\alpha$  and  $\beta$ , and the coefficient of determination  $R^2$ , are presented in Table II.  $R^2$  values show a better fit to the gold standard PET when the pCT  $\mu$ -map is used to correct for attenuation instead of the baCT or the UTE  $\mu$ -maps. Fig. 8 shows the joint histograms, averaged across 41 subjects, of the pCT, baCT, UTE, and noncorrected PETs against the gold standard PET. We note that the pseudo CT method outperforms the UTE method and that the variance is reduced when the PET is corrected by the pCT instead of the baCT  $\mu$ -map.

Finally, the PET images from the 41 subjects were mapped to a common space via a CT-based groupwise registration [38]. The average and standard deviation of the difference maps computed between the normalized gold standard PETs and the normalized PETs reconstructed with the pseudo CT, best-atlas and UTE  $\mu$ -maps, across all the subjects, are presented in Fig. 9. We note that, while the average of the difference between the gold standard and both the pCT PETs and baCT PETs is similar, the

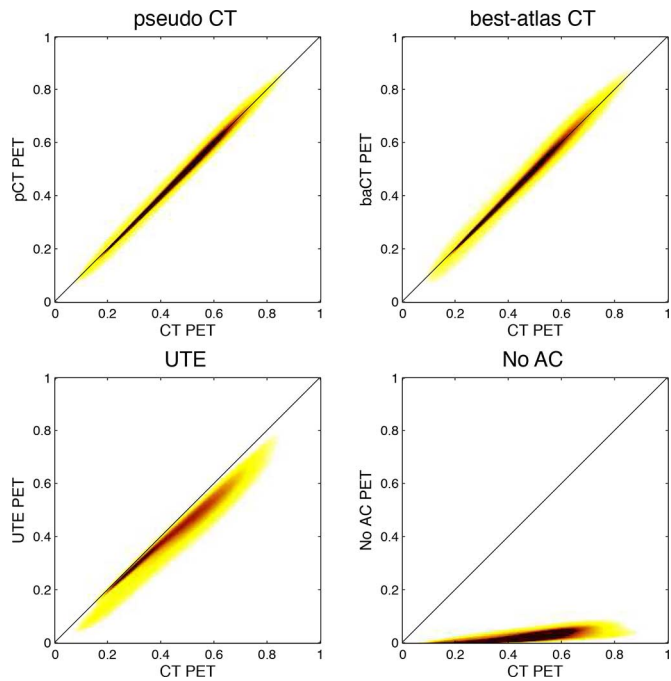


Fig. 8. Joint histograms in the brain area, averaged across 41 subjects, between the CT and pCT PETs (top left), the CT and baCT PETs (top right), the CT and UTE PETs (bottom left), and the CT and noncorrected PETs (bottom right). Images are min/max scaled between 0 and 1. Note the reduced variance when the PET is corrected using the proposed method compared to the best-atlas method.

TABLE II

FOR 41 SUBJECTS: AVERAGE  $\pm$  SD OF THE REGRESSION COEFFICIENTS AND  $R^2$  VALUES COMPUTED IN THE BRAIN AREA FOR THE PROPOSED (pCT), BEST-ATLAS (baCT), AND UTE-BASED (UTE) METHODS, AND WITHOUT CORRECTION (NO AC). NOTE THE INCREASE IN  $R^2$  WITH THE PROPOSED APPROACH WHEN COMPARED TO OTHER METHODS

	pCT	baCT	UTE	No AC
$\alpha$	$1.009 \pm 0.021$	$1.018 \pm 0.028$	$0.905 \pm 0.033$	$0.088 \pm 0.007$
$\beta$	$-83.0 \pm 153.4$	$-111.8 \pm 242.3$	$-317.9 \pm 390.1$	$-374.65 \pm 120.0$
$R^2$	$0.988 \pm 0.005$	$0.973 \pm 0.014$	$0.944 \pm 0.014$	$0.601 \pm 0.048$

standard deviation of the difference between the gold standard and pCT PETs (2.36%) is lower than between the gold standard and baCT PETs (3.97%).

5) *Example of PET Reconstruction From Sinogram Data:* As a final test for the performance of the method, we used an offline version of the Siemens Healthcare reconstruction software (made available for this project) on PET/MR data for one subject from the validation dataset. The default settings for OSEM (21 iterations of three subsets, Gaussian post-filtering) were used. We reconstructed PET images using the CT, pCT, baCT, and the UTE  $\mu$ -maps to correct for attenuation. Results are shown in Fig. 10. The UTE-based method underestimates the quantity of bone which leads to a global underestimation of the activity in the PET image. Compared to the proposed method, the best-atlas method sometimes fails to accurately delineate the bone, such as in the skull (yellow arrows) and sinus areas (green arrow), which results in a local underestimation of the PET activity. The rMAE, computed for the full head, is of 5.0% between the pCT and CT PETs, 5.6% between the baCT and CT PETs, and 12.2% between the UTE and CT PETs.

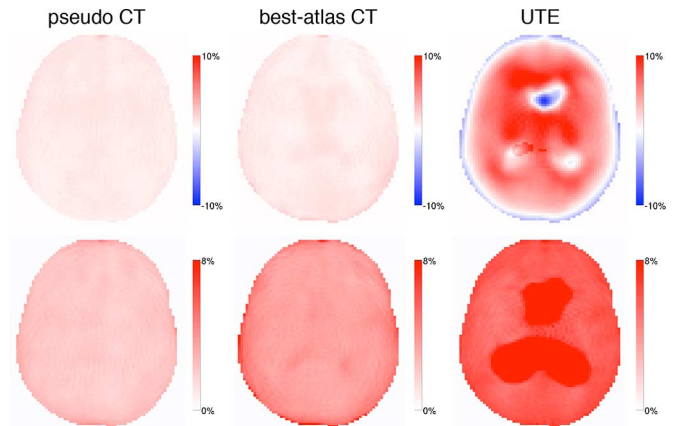


Fig. 9. Average over 41 subjects (top) and standard deviation (bottom) of the difference between the normalized gold standard PET and the normalized PETs reconstructed with the pseudo CT, best-atlas and UTE  $\mu$ -maps.

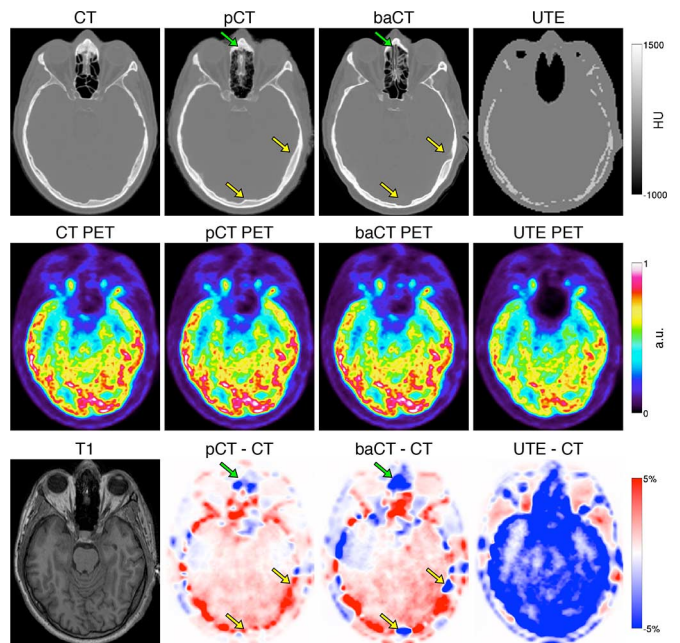


Fig. 10. From left to right: The CT  $\mu$ -map, the pCT  $\mu$ -map generated by the proposed method, the baCT  $\mu$ -map and the UTE  $\mu$ -map (top row). Gold standard FDG PET, pCT PET, baCT PET, and UTE PET reconstructed with the offline Siemens Healthcare software (middle row). The T1, the difference between the pCT and CT PETs, the baCT and CT PETs, and the UTE and CT PETs (bottom row).

#### IV. DISCUSSION

Following the principle of multi-atlas information propagation, the proposed method synthesizes a CT from an MRI image which is then processed to obtain an attenuation map used in the PET reconstruction.

Two separate datasets were used for the optimization and the validation of the method to reduce bias. We compared our solution to a simpler atlas-based method and to a prototype version of a UTE-based method made available to early users of the Siemens Biograph mMR hybrid PET/MR scanners. The results presented in Table I demonstrate that the absolute error estimated between the pseudo CT and the original CT is significantly smaller compared to the other methods. Difference

images in Fig. 3 reveal that errors are concentrated at the skull/soft-tissue, skull/air, and soft-tissue/air boundaries, and that the amount of bone is underestimated when the UTE-based method is used. We also notice in Fig. 3 that the synthetic CT images are not as sharp as the ground-truth subject's CT at the original resolution. However, this problem is greatly reduced at the voxel size and PSF of the PET image as shown in Fig. 4. At this resolution, the results show a significant improvement when our method is used compared to the best-atlas and UTE-based methods. Difference images of reconstructed PET images from simulated data in Fig. 5 show that the UTE-based correction underestimates the radionuclide uptake, even for the soft-tissues. This systematic underestimation is confirmed by the joint histogram Fig. 8 and the linear regression coefficients in Table II. When the PET is corrected with the pseudo CT or best-atlas  $\mu$ -map, the error is globally lower and mostly affects the skull and sinus areas. Finally, the error is significantly smaller with the pseudo CT method compared to the best-atlas CT method and the bias lower. After normalization, the error obtained with the UTE-based method is reduced while it remains alike for the proposed and best-atlas methods. All correction methods introduce a bias but the variance of the bias is significantly lower when the pseudo CT method is used instead of the best-atlas or UTE method, as shown in Table I and Fig. 9.

The use of the Siemens offline reconstruction software is still at an early stage but already demonstrates that the proposed method improves the results when applied in a clinical context compared to the method currently in use, as shown in Fig. 10.

In a T1-weighted MRI image of the head, cerebrospinal fluid, air, and bone have similar intensities but distinct values in a CT image which impedes a one-to-one mapping from the observed MRI intensities to CT-like intensities. Exploiting the concept of morphological similarity between subjects, as an alternative to the one-to-one intensity mapping, improves the synthesis accuracy in boundary areas such as air and bone in the nasal sinuses. The low intensities of bone and air also make the segmentation of MRI images challenging [6]–[12], even after correction of several artefacts [10]. The proposed method does not require any segmentation of MRI images and thus allows the synthesis of a continuous valued attenuation map and avoids large misclassifications.

However, atlas-based methods also have limitations as relying on a database implies the need of a representative population. But, even if morphological variabilities of the skull are limited, in the case where the target subject presents abnormalities, the nonrigid registration should be able to capture them. Further experiments with subjects presenting abnormal anatomies are required to validate this expectation. Although large number of registrations can leave room for errors to confound the mapping in a single atlas method, the proposed multi-atlas strategy can compensate for most registration problems by combining the local atlas selection and consensus estimation steps. The more accurate results reached when the proposed method is used, compared to the best-atlas method, demonstrate the advantages of synthesizing CTs at a local scale instead of a global scale.

Current limitations of the method are due to the limited anatomical information of CT and T1-weighted MRI images. A database with multimodal data including T1-weighted,

T2-weighted, and UTE sequences would improve the registration and the image similarity estimates, and could provide additional information, such as bone density. Clinical information (patient's gender, age, weight, or ethnicity) could also be used to specify the bone density more accurately [18].

This paper is focused on brain applications and further experiments are required to validate the method in other regions of the body. The technique could, in theory, be applied to other body parts as long as the morphological variability is represented in the database and the registration between MRI pairs is sufficiently accurate.

The software implementing the proposed method will be made available online at the time of publication.

## V. CONCLUSION

This paper presents a CT and attenuation map synthesis algorithm based on a multi-atlas information propagation scheme. Compared to state-of-the-art image synthesis techniques, the proposed technique does not assume any explicit mapping between the intensities of the image pairs, as it relies only on their correct pre-alignment. While the sharpness of the synthetic CT images is lower than the ground-truth subject's CT at the original resolution, this problem is greatly reduced at the resolution of the PET image. Overall, the proposed algorithm provides a significant improvement in PET reconstruction accuracy when compared to a simplified atlas-based or UTE-based correction.

## ACKNOWLEDGMENT

The authors would like to thank C. Hutton and J. Declerck for their comments on the overall work.

## REFERENCES

- [1] G. K. von Schulthess, F. P. Kuhn, P. Kaufmann, and P. Veit-Haibach, "Clinical positron emission tomography/magnetic resonance imaging applications," *Seminars Nucl. Med.*, vol. 43, no. 1, pp. 3–10, 2013.
- [2] I. Bezrukov, F. Mantlik, H. Schmidt, B. Schölkopf, and B. J. Pichler, "MR-based PET attenuation correction for PET/MR imaging," *Seminars Nucl. Med.*, vol. 43, no. 1, pp. 45–59, 2013.
- [3] A. Salomon, A. Goedicke, B. Schweizer, T. Aach, and V. Schulz, "Simultaneous reconstruction of activity and attenuation for PET/MR," *IEEE Trans. Med. Imag.*, vol. 30, no. 3, pp. 804–813, Mar. 2011.
- [4] R. Boellaard, M. Hofman, O. Hoekstra, and A. Lammertsma, "Accurate PET/MR quantification using time of flight MLAA image reconstruction," *Mol. Imag. Biol.*, pp. 1–9, 2014.
- [5] A. Rezaei, M. Defrise, G. Bal, C. Michel, M. Conti, C. Watson, and J. Nuyts, "Simultaneous reconstruction of activity and attenuation in time-of-flight PET," *IEEE Trans. Med. Imag.*, vol. 31, no. 12, pp. 2224–2233, Dec. 2012.
- [6] A. Martinez-Möller, M. Souvatzoglou, G. Delso, R. A. Bundschuh, C. Chefd'hotel, S. I. Ziegler, N. Navab, M. Schwaiger, and S. G. Nekolla, "Tissue classification as a potential approach for attenuation correction in whole-body PET/MRI: evaluation with PET/CT data," *J. Nucl. Med.*, vol. 50, no. 4, pp. 520–526, 2009.
- [7] P. J. Schleyer, T. Schaeffter, and P. K. Marsden, "The effect of inaccurate bone attenuation coefficient and segmentation on reconstructed PET images," *Nucl. Med. Commun.*, vol. 31, no. 8, pp. 708–716, 2010.
- [8] C. Catana, A. van der Kouwe, T. Benner, C. J. Michel, M. Hamm, M. Fenchel, B. Fischl, B. Rosen, M. Schmand, and A. G. Sorensen, "Toward implementing an MRI-based PET attenuation-correction method for neurologic studies on the MR-PET brain prototype," *J. Nucl. Med.*, vol. 51, no. 9, pp. 1431–1438, 2010.
- [9] V. Keereman, Y. Fierens, T. Broux, Y. De Deene, M. Lonnew, and S. Vandenberghe, "MRI-based attenuation correction for PET/MRI using ultrashort echo time sequences," *J. Nucl. Med.*, vol. 51, no. 5, pp. 812–818, 2010.

- [10] A. P. Aitken, D. Giese, C. Tsoumpas, P. Schleyer, S. Kozierke, C. Prieto, and T. Schaeffter, "Improved UTE-based attenuation correction for cranial PET-MR using dynamic magnetic field monitoring," *Med. Phys.*, vol. 41, no. 1, p. 012302, 2014.
- [11] Y. Berker, J. Franke, A. Salomon, M. Palmowski, H. C. W. Donker, Y. Temur, F. M. Mottaghy, C. Kuhl, D. Izquierdo-Garcia, Z. A. Fayad, F. Kiessling, and V. Schulz, "MRI-based attenuation correction for hybrid PET/MRI systems: A 4-class tissue segmentation technique using a combined ultrashort-echo-time/Dixon MRI sequence," *J. Nucl. Med.*, vol. 53, no. 5, pp. 796–804, 2012.
- [12] X. Yang and B. Fei, "Multiscale segmentation of the skull in MR images for MRI-based attenuation correction of combined MR/PET," *J. Am. Med. Informat. Assoc.*, pp. 1–9, 2013.
- [13] E. Schreiber, J. A. Nye, D. M. Schuster, D. R. Martin, J. Votaw, and T. Fox, "MR-based attenuation correction for hybrid PET-MR brain imaging systems using deformable image registration," *Med. Phys.*, vol. 37, no. 5, p. 2101, 2010.
- [14] A. Johansson, M. Karlsson, and T. Nyholm, "CT substitute derived from MRI sequences with ultrashort echo time," *Med. Phys.*, vol. 38, no. 5, p. 2708, 2011.
- [15] A. Johansson, A. Garpebring, M. Karlsson, T. Asklund, and T. Nyholm, "Improved quality of computed tomography substitute derived from magnetic resonance (MR) data by incorporation of spatial information-potential application for MR-only radiotherapy and attenuation correction in positron emission tomography," *Acta Oncologica*, vol. 52, no. 7, pp. 1369–1373, 2013.
- [16] M. Hofmann, F. Steinke, V. Scheel, G. Charpiat, J. Farquhar, P. Aschoff, M. Brady, B. Schölkopf, and B. J. Pichler, "MRI-based attenuation correction for PET/MRI: A novel approach combining pattern recognition and atlas registration," *J. Nucl. Med.*, vol. 49, no. 11, pp. 1875–1883, 2008.
- [17] B. K. Navalpakkam, H. Braun, T. Kuwert, and H. H. Quick, "Magnetic resonance-based attenuation correction for PET/MR hybrid imaging using continuous valued attenuation maps," *Invest. Radiol.*, vol. 48, no. 5, pp. 323–332, 2013.
- [18] H. R. Marshall, J. Patrick, D. Laidley, F. S. Prato, J. Butler, J. Théberge, R. T. Thompson, and R. Z. Stodilka, "Description and assessment of a registration-based approach to include bones for attenuation correction of whole-body PET/MRI," *Med. Phys.*, vol. 40, no. 8, p. 082509, 2013.
- [19] F. L. Andersen, C. N. Ladefoged, T. Beyer, S. H. Keller, A. E. Hansen, L. Højgaard, A. Kjær, I. Law, and S. Holm, "Combined PET/MR imaging in neurology: MR-based attenuation correction implies a strong spatial bias when ignoring bone," *NeuroImage*, vol. 84, pp. 206–216, 2014.
- [20] J. C. Dickson, C. O'Meara, and A. Barnes, "A comparison of CT- and MR-based attenuation correction in neurological PET," *Eur. J. Nucl. Med. Mol. Imag.*, 2014.
- [21] R. A. Heckemann, J. V. Hajnal, P. Aljabar, D. Rueckert, and A. Hammers, "Automatic anatomical brain MRI segmentation combining label propagation and decision fusion," *NeuroImage*, vol. 33, no. 1, pp. 115–126, 2006.
- [22] M. R. Sabuncu, K. VanLeemput, B. Fischl, and P. Golland, "A generative model for image segmentation based on label fusion," *IEEE Trans. Med. Imag.*, vol. 29, no. 10, pp. 1714–1729, Oct. 2010.
- [23] N. Burgos, M. Cardoso, M. Modat, S. Pedemonte, J. Dickson, A. Barnes, J. S. Duncan, D. Atkinson, S. R. Arridge, B. F. Hutton, and S. Ourselin, "Attenuation correction synthesis for hybrid PET-MR scanners," in *Proc. MICCAI*, 2013, pp. 147–154.
- [24] J. G. Sled, A. P. Zijdenbos, and A. C. Evans, "A nonparametric method for automatic correction of intensity nonuniformity in MRI data," *IEEE Trans. Med. Imag.*, vol. 17, no. 1, pp. 87–97, Feb. 1998.
- [25] M. Modat, D. M. Cash, P. Daga, G. P. Winston, J. S. Duncan, and S. Ourselin, "A symmetric block-matching framework for global registration," in *Proc. SPIE Med. Imag.*, 2014, vol. 9034, p. 90341D.
- [26] S. Ourselin, A. Roche, and G. Subsol, "Reconstructing a 3D structure from serial histological sections," *Image Vis. Comput.*, vol. 19, no. 2000, pp. 25–31, 2001.
- [27] M. Modat, G. R. Ridgway, Z. A. Taylor, M. Lehmann, J. Barnes, D. J. Hawkes, N. C. Fox, and S. Ourselin, "Fast free-form deformation using graphics processing units," *Comput. Methods Programs Biomed.*, vol. 98, no. 3, pp. 278–284, 2010.
- [28] P. Cachier, E. Bardinet, D. Dormont, X. Pennec, and N. Ayache, "Iconic feature based nonrigid registration: The PASHA algorithm," *Comput. Vis. Image Understand.*, vol. 89, no. 2–3, pp. 272–298, 2003.
- [29] P. A. Yushkevich, H. Wang, J. Pluta, S. R. Das, C. Craige, B. B. Avants, M. W. Weiner, and S. Mueller, "Nearly automatic segmentation of hippocampal subfields in in vivo focal T2-weighted MRI," *NeuroImage*, vol. 53, no. 4, pp. 1208–24, 2010.
- [30] M. Cardoso, R. Wolz, M. Modat, N. C. Fox, D. Rueckert, and S. Ourselin, "Geodesic information flows," in *Proc. MICCAI*, 2012, vol. 7511, pp. 262–270.
- [31] C. Burger, G. Goerres, S. Schoenes, A. Buck, A. H. R. Lonn, and G. K. Von Schulthess, "PET attenuation coefficients from CT images: Experimental evaluation of the transformation of CT into PET 511-keV attenuation coefficients," *Eur. J. Nucl. Med. Mol. Imag.*, vol. 29, no. 7, pp. 922–927, 2002.
- [32] M. R. Ay, M. Shirmohammad, S. Sarkar, A. Rahmim, and H. Zaidi, "Comparative assessment of energy-mapping approaches in CT-based attenuation correction for PET," *Mol. Imag. Biol.*, vol. 13, no. 1, pp. 187–198, 2011.
- [33] C. Watson, "New, faster, image-based scatter correction for 3D PET," *IEEE Trans. Nucl. Sci.*, vol. 47, no. 4, pp. 1587–1594, Aug. 2000.
- [34] K. Thielemans, C. Tsoumpas, S. Mustafovic, T. Beisel, P. Aguiar, N. Dikaio, and M. W. Jacobson, "STIR: Software for tomographic image reconstruction release 2," *Phys. Med. Biol.*, vol. 57, no. 4, pp. 867–83, 2012.
- [35] S. Minoshima, K. A. Frey, N. L. Foster, and D. E. Kuhl, "Preserved pontine glucose metabolism in alzheimer disease a reference region for functional brain image (PET) analysis," *J. Comput. Assist. Tomogr.*, vol. 19, no. 4, pp. 541–547, 1995.
- [36] E. M. Lee, G. Y. Park, K. C. Im, S. T. Kim, C.-W. Woo, J. H. Chung, K. S. Kim, J. S. Kim, Y.-M. Shon, Y. I. Kim, and J. K. Kang, "Changes in glucose metabolism and metabolites during the epileptogenic process in the lithium-pilocarpine model of epilepsy," *Epilepsia*, vol. 53, no. 5, pp. 860–869, 2012.
- [37] M. J. Cardoso, M. J. Clarkson, G. R. Ridgway, M. Modat, N. C. Fox, and S. Ourselin, "LoAd: A locally adaptive cortical segmentation algorithm," *NeuroImage*, vol. 56, no. 3, pp. 1386–1397, 2011.
- [38] T. Rohlfing, R. Brandt, J. Maurer, C. R., and R. Menzel, "Bee brains, B-splines and computational democracy: Generating an average shape atlas," in *Proc. IEEE Workshop Math. Methods Biomed. Image Anal.*, 2001, pp. 187–194.